

# Superconductivity from a melted insulator

S. Mukhopadhyay,<sup>1,\*</sup> J. Senior,<sup>1,\*</sup> J. Saez-Mollejo,<sup>1</sup> D. Puglia,<sup>1</sup> M. Zemlicka,<sup>1</sup> J. Fink,<sup>1</sup> and A.P. Higginbotham<sup>1,†</sup>

<sup>1</sup>*IST Austria, Am Campus 1, 3400 Klosterneuburg, Austria*

Quantum phase transitions typically result in a broadened critical or crossover region at nonzero temperature [1]. Josephson arrays are a model of this phenomenon [2], exhibiting a superconductor-insulator transition at a critical wave impedance [3–13], and a well-understood insulating phase [14, 15]. Yet high-impedance arrays used in quantum computing [16–19] and metrology [20] apparently evade this transition, displaying superconducting behavior deep into the nominally insulating regime [21]. The absence of critical behavior in such devices is not well understood. Here we show that, unlike the typical quantum-critical broadening scenario, in Josephson arrays temperature dramatically shifts the critical region. This shift leads to a regime of superconductivity at high temperature, arising from the melted zero-temperature insulator. Our results quantitatively explain the low-temperature onset of superconductivity in nominally insulating regimes, and the transition to the strongly insulating phase. We further present, to our knowledge, the first understanding of the onset of anomalous-metallic resistance saturation [22]. This work demonstrates a non-trivial interplay between thermal effects and quantum criticality. A practical consequence is that, counterintuitively, the coherence of high-impedance quantum circuits is expected to be stabilized by thermal fluctuations.

Josephson-array superinductors are characterized by a Josephson energy  $E_J$ , junction charging energy  $E_C$ , and ground charging energy  $E_g$  [17]. A common experimental strategy for avoiding insulating behavior is to make the fugacity for quantum phase slips  $y \propto e^{-4\sqrt{2E_J/E_C}}$  small. However, for high-impedance arrays the fugacity is always renormalized towards infinity as temperature goes to zero [13, 23], resulting in insulating behavior. Our key insight is that long superinductors avoid this fate by operating above the melting point of the insulating phase, where the low-temperature renormalization has yet to occur, and that this results in apparent superconducting behavior. This effect quantitatively explains the presence of superconducting behavior, resistance saturation, and transition to strongly insulating regimes in superinductors.

Two nearly identical devices are studied: one galvanically coupled to electrical leads permitting the measurement of resistance, and one capacitively coupled to mi-

crowave transmission lines permitting the measurement of plasma modes [17, 21]. Both devices consist of an array of approximately 1220 Josephson junctions fabricated using electron-beam lithography and a standard shadow evaporation process on high-resistivity silicon substrates (Fig. 1a) [24]. For nanofabrication reasons the array islands have alternating thickness, which, in the presence of magnetic field, should give rise to an alternating gap structure while maintaining a uniform Josephson energy throughout the chain. At zero magnetic field, each junction has nominally identical  $E_J/h \approx 76$  GHz,  $E_g/h \approx 1400$  GHz, and  $E_C/h \approx 5$  GHz. These parameters are determined from analyzing microwave ( $E_J, E_g$ ) and transport ( $E_C$ ) measurements with several consistency checks, as described below and in the Supplement [24].

The working principle of the experiment is to leverage the complementary strengths of low-frequency electrical transport and microwave-domain circuit quantum electrodynamics. These techniques differ by nine orders of magnitude in characteristic frequency, and combine to give access to both the scaling behavior, associated with low energies (transport), and the microscopic system parameters, associated with high energies (microwave).

In the transport device, a linear current-voltage characteristic at large applied voltage bias gives way to a high resistance region at low bias, whose extent is approximately given by the number of junctions  $N$  times twice the superconducting gap  $\Delta$  (Fig. 1b). Over a smaller range of applied voltage a series of evenly spaced current peaks are observed with an apparent supercurrent at zero bias (Fig. 1b inset). The successive current peaks can be qualitatively understood within a picture of successive voltage drops across  $N$  voltage-biased Josephson junctions, with low current on the quasiparticle branches and high current when bias is a multiple of  $2\Delta/e$  [11].

Increasing magnetic field  $B$  parallel to the chip plane suppresses supercurrent, suggesting a field-driven transition from a superconducting to an insulating state (Fig. 1c). The spacing between current peaks also decreases with  $B$ , indicating a reduction in the superconducting gap with magnetic field. In the strongly superconducting regime ( $B = 0$ ), zero-bias differential resistance per junction (specific resistance) associated with the superconducting branch decreases dramatically with cryostat temperature (Fig. 1d), dropping over more than three decades before saturating to a low value of  $< 1 \Omega$  per junction. Due to the long length of the array, we rule out finite-size effects as a possible origin of the low-temperature saturation [25]. The precipitous drop in re-

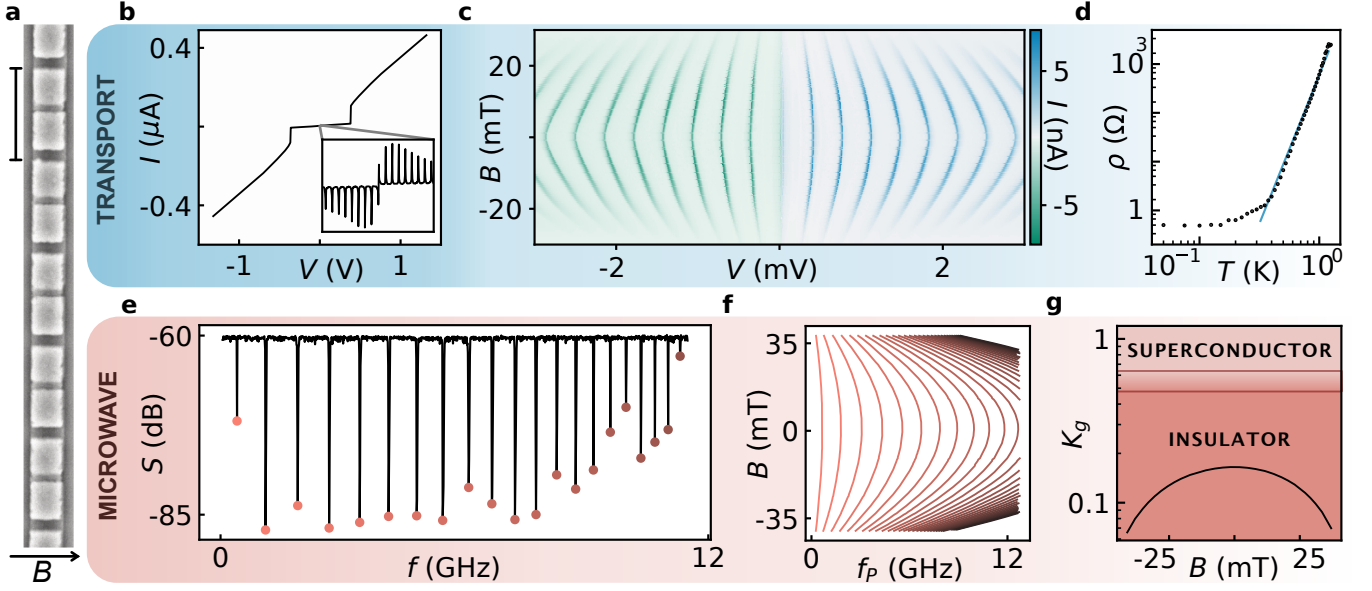


**Figure 1: Device, transport, and microwave measurement techniques.** **a**, Scanning electron micrograph of a small segment of the Josephson array. Left scale bar indicates  $1.5 \mu\text{m}$ . Arrow indicates direction of magnetic field  $B$ . **b**, Current  $I$  versus source-drain bias voltage  $V$ . Inset shows small-scale current peaks over a narrow range  $(-3, 3)$  mV. **c**, Current  $I$  versus bias  $V$  and magnetic field  $B$  over a bias range similar to Fig. 1b inset. **d**, Differential resistance per junction (specific resistance)  $\rho$  versus cryostat temperature  $T$  measured at  $V = 0$  and  $B = 0$ . Blue line shows power-law fit.  $\rho$  reflects the resistance associated with the zero-bias superconducting branch, found by measuring the two-probe resistance, subtracting off four-probe-measured line resistance, and then dividing by number of junctions. **e**, Two-tone microwave spectroscopy. Probe tone transmission  $S$  versus pump-tone frequency  $f$ , with probe tone frequency fixed to resonance at approximately 6.11 GHz. Extracted plasma-mode resonant frequencies  $f_P$  indicated by colored markers. **f**, Evolution of measured plasma-mode frequencies  $f_P$  with applied magnetic field  $B$ . **g**, Superfluid stiffness  $K_g = \sqrt{E_J/(2E_g)}$ , experimentally inferred from plasma modes in **f**, versus  $B$  (black line). Theoretically expected superconducting and insulating regimes labeled, and demarcated by a band covering the clean [2] and dirty [23] limits.

sistance at low temperature and supercurrent features in nonlinear transport give a preliminary indication of the dominance of superconducting behavior. We will develop a framework for understanding the behavior of specific resistance in detail, but first turn to the complementary use of microwave techniques to independently determine system parameters.

Microwave spectroscopy is performed by monitoring the transmission of a weak probe signal while the frequency of a strong pump tone is varied [17]. A series of sharp dips are observed in probe-tone transmission  $S$  (Fig. 1e), corresponding to plasma modes of the array. The plasma modes are evenly spaced at low frequency, reflecting the speed of light and length of the array, and are clustered at high frequency due to proximity with the single-junction plasma frequency. A simple fitting procedure allows extraction of the array parameters from the microwave data [24]. Performing two-tone spectroscopy as a function of field (Fig. 1f), the array parameters  $E_g$ ,  $E_C$ , and  $E_J(B)$  are fully characterized as a function of magnetic field. With these values fixed experimentally, it

is straightforward to perform parameter-free comparisons with the theory of the superconductor-insulator transition in one dimension.

Performing this comparison (Fig. 1g) reveals that the array's superfluid stiffness  $K_g = \sqrt{E_J/(2E_g)}$  is as much as an order of magnitude below the critical value for insulating behavior [2, 23], in contrast to the observed superconducting behavior in transport. Thus, combining the transport and microwave measurements reveals an apparent conflict with basic expectations for the superconductor-insulator phase transition. Resolving this conflict is the central subject of this work.

The theoretical picture for understanding our observations was developed in Ref. [13]. Near the superconductor-insulator transition, thermal fluctuations are controlled by the timescale  $\tau = \hbar/k_B T$  and the associated thermal length  $l_{\text{th}} = v\tau$ , where  $v$  is a characteristic velocity with dimensions of unit cells per time.  $l_{\text{th}}$  must be compared with the electrostatic screening length in units of unit cells,  $\Lambda = \sqrt{E_g/E_C}$ . At high temperature ( $l_{\text{th}} < \Lambda$ ) the system is governed by the local superfluid

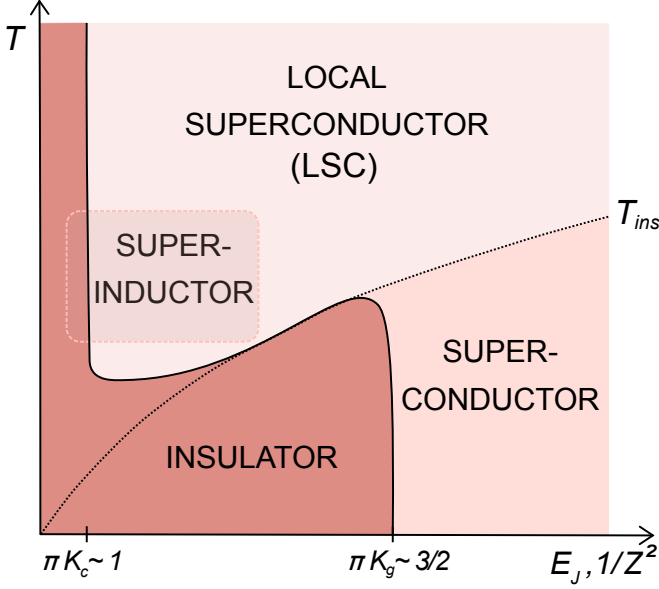


**Figure 2: Proposed phase diagram.** Map of superconducting and insulating states as a function of Josephson energy  $E_J$  and temperature  $T$ . Dashed line marks the boundary between long-range and short-range behavior,  $T_{\text{ins}}$ , given by Eq. 1. Below  $T_{\text{ins}}$ , physics is governed by the long-range superfluid stiffness  $K_g$  with a superconductor-insulator transition at  $\pi K_g \sim 3/2$ . Above  $T_{\text{ins}}$ , physics is governed by the short-range superfluid stiffness  $K_C$  with a superconductor-insulator transition as  $\pi K_C \sim 1$ . Solid black curve traces the crossover from local to global superconductor-insulator transition. Outlined box indicates superinductance region probed in this experiment.

stiffness,  $K_C = \sqrt{E_J/(2E_C)}$ . In contrast, at low temperature ( $t_{\text{th}} > \Lambda$ ) the system is governed by the long-range superfluid stiffness  $K_g$ , as assumed by standard theories of the superconductor-insulator transition. In the superinductor limit superconductivity is locally stiff,  $K_C \gg K_g$ , which results in a curious regime of local superconductivity that arises from a melted  $T = 0$  insulator (Fig. 2). The “melting point” of the insulator, above which local superconductivity dominates, is

$$T_{\text{ins}} \sim \sqrt{2E_J E_C}/\Lambda. \quad (1)$$

In the locally superconducting regime, we find that the high-temperature behavior of the specific resistance follows a power law

$$\rho = \rho_0 (T/T_p)^{\pi K_C - 1}, \quad (2)$$

where  $T_p = \sqrt{2E_J E_C}/k_B$  is the plasma temperature [24]. Local superconductivity gives way to insulating behavior when  $\pi K_C \sim 1$ . In contrast, in the low-temperature limit the power law is  $2\pi K_g - 3$ , which yields the typical superconductor-insulator prediction  $\pi K_g \sim 3/2$ .

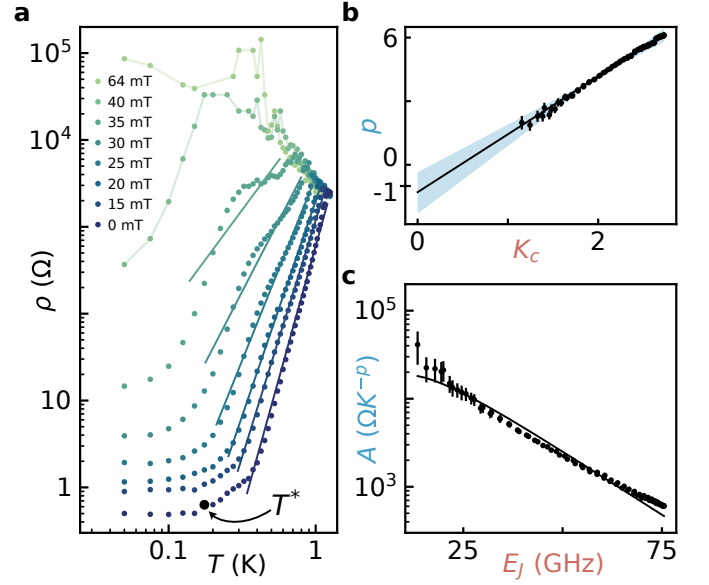


**Figure 3: Power law nature of local superconductivity.** **a**, Zero-bias specific differential resistance  $\rho$  as a function of temperature  $T$ , at various magnetic fields. Solid lines are fits to power law expression  $\rho = AT^p$ .  $T^*$  is the crossover temperature from power law to saturation behavior, extracted from the point where specific resistance goes 20% above its minimum value. **b**, Exponent  $p$  from power-law fits to transport data in **a** versus the local superfluid stiffness  $K_C$  from microwave measurements. Solid line is a linear fit. Shaded blue region in **b** depicts the systematic error resulting from the choice of lower resistance cutoff in the power law fits [24]. **c**, Amplitude  $A$  from power-law fits to transport data versus Josephson energy  $E_J$  from microwave measurements.

The experimentally studied devices have, at  $B = 0$ ,  $\pi K_g < 1 < \pi K_C$ , and  $T_{\text{ins}} \sim 70$  mK, giving an initial suggestion that they are governed by local superconductivity even at low temperatures. This hypothesis can be tested by comparing experimental measurements of temperature dependent specific resistance,  $\rho(T)$ , with the predicted power law in Eq. 2. As shown in Fig. 3a, increasing magnetic field weakens the temperature dependence of the specific resistance, eventually giving way to a superconductor insulator transition at high magnetic field ( $B \sim 44$  mT). Fitting each specific resistance curve to a power law  $\rho = AT^p$  indicates that, on the superconducting side, the exponent  $p$  steadily decreases with field. Comparing  $p$  from the transport measurements with the local superfluid stiffness  $K_C$  inferred from microwave measurements reveals a linear behavior (Fig. 3b) with slope  $2.7 \pm 0.50$  and intercept of  $-1.3 \pm 1.0$ , in agreement with the predicted slope  $\pi$  and intercept  $-1$  for local superconductivity from Eq. 2,  $p = \pi K_C - 1$  [26]. We

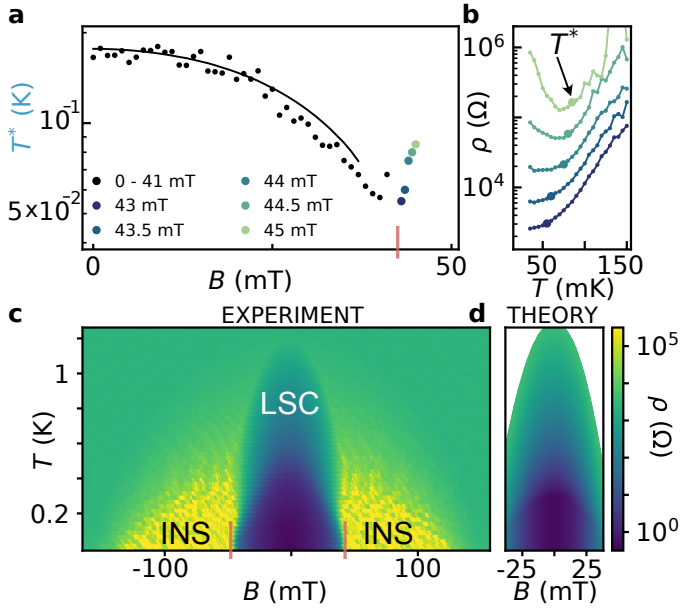


**Figure 4: Crossover physics and phase diagram.** **a**, Crossover temperature  $T^*$  versus magnetic field  $B$ . Black line is  $T^* \propto T_{\text{ins}}$  with a proportionality constant of 2.2. Colored markers indicate crossover temperature at higher fields from dataset in **b**. Red vertical line indicates  $\pi K_C = 1$ , where local superconductor-insulator transition is expected. **b**, Zero-bias differential specific resistance  $\rho$  versus temperature  $T$  at higher magnetic fields, measured with higher excitation voltage and more averaging than in Fig. 3. **c**,  $\rho$  versus temperature  $T$  and magnetic field  $B$ . Dome of local superconductivity (LSC), and wings of insulating behavior (INS) labeled. Red vertical lines indicate  $\pi K_C = 1$ , where local superconductor-insulator transition is expected. **d**, Calculated specific resistance  $\rho$  as a function of temperature  $T$  and magnetic field  $B$ .

note that, near the superconductor-insulator transition, power-law behavior is interrupted by a shoulder-like feature at high temperature, which is not understood. Amplitude dependence on  $E_J$  (Fig. 3c) is also in reasonable agreement with the prediction of Eq. 2,  $A = \rho_0/T_p^{\pi K_C - 1}$ , with a single free parameter,  $\rho_0 = 4.8 \pm 0.30$  k $\Omega$ , which is of the order of single-junction normal-state resistance. Experimental agreement with Eq. 2 gives strong evidence that superconductivity is local, and resolves the apparent paradox of superconductivity at low  $K_g$  suggested by Fig. 1g.

The boundaries of local superconductivity can also be understood within the picture of Fig. 2. At low temperatures, the experimentally observed power-law behavior in resistance saturates at a crossover temperature  $T^*$  (indicated in Fig. 3a). The crossover temperature decreases with magnetic field, as shown in Fig. 4a, agreeing with the expected square-root dependence for  $T^* \propto T_{\text{ins}}$ ,

which supports the view that the low-temperature saturation is in fact a crossover into the insulating state. At high magnetic fields corresponding to  $\pi K_C > 1$ ,  $T^*$  increases with magnetic field (Fig. 4b), consistent with a superconductor-insulator transition entering into the non-perturbative insulating regime of Ref. [13], where the phase-slip fugacity,  $\propto e^{-8\sqrt{E_J/E_C}}$ , is no longer small. We caution that the experimental interpretation of  $T^*$  is complicated for two reasons. First, although we have performed normal-state electron thermometry and radiation thermometry and found that all characteristic temperatures are below  $T^*$ , thermalization at the actual superconductor-insulator transition is difficult to verify directly. Second, different metrics for  $T^*$  give quantitatively different scaling with  $B$ , although the decreasing trend predicted by Eq. 1 is a robust feature.

The complete behavior of the Josephson array can be summarized by measuring a resistance “phase diagram.” Mapping zero-bias differential resistance as a function of magnetic field and temperature reveals a characteristic dome at low field, already identified from the power-law analysis as a local superconductor, giving way to a high-resistance insulating phase as magnetic field is increased (Fig. 4c). The low-temperature boundary between superconducting and insulating states occurs at  $\pi K_C \sim 1$ , as expected. We speculate that the high-field boundary of the high-resistance regime corresponds to the upper critical field of the thinnest islands of the array.

The local superconducting dome and its boundaries can be quantitatively modeled as follows. The thermal boundary of the dome is  $T = T_p$ , the upper cut-off scale of our renormalization-group approach [13]. For  $\alpha T_{\text{ins}} < T < T_p$  Eq. 2 applies, with  $\rho_0$  from Fig. 3c. For  $T < \alpha T_{\text{ins}}$  resistance saturates due to a crossover into the insulating regime, and would presumably increase at lower, experimentally inaccessible temperatures. The constant  $\alpha = 5$ , which tunes the crossover to insulating behavior in the model, is fixed from the experimentally observed saturation resistance at  $B = 0$  and in reasonable agreement with the constant found in Fig. 4a. For sufficiently large  $B$  one approaches  $\pi K_C = 1$ , which sets the magnetic field boundaries of the dome. Calculating  $\rho$  according to this procedure results in a local superconducting dome in satisfactory agreement to the experiment (Fig. 4d). This gives evidence that the presence of local superconductivity, and its proximity to insulating phases, is well understood.

Summarizing, by combining transport and microwave measurements, we have uncovered strong evidence for a locally superconducting state in Josephson arrays arising from a  $T = 0$  insulator. This resolves the problem of apparent superconductivity in nominally insulating regimes, and clarifies where superconductor-insulator transitions are actually observed in experiment. Our work sheds new light on the observation of high-quality



microwave response in the nominally insulating regime of superinductors [21], suggesting effects in addition to high-frequency mechanisms that have been previously discussed [27–29]. Such devices operate near the “sweet spot”  $T \approx T_{\text{ins}}$  where temperature is low enough for well-developed local superconductivity, yet high enough to melt insulating behavior. As a consequence, we suggest that the performance of some high-impedance quantum devices [18, 19, 30] is actually improved by thermal fluctuations. It is also interesting to consider if experimental studies of insulating behavior in resistively shunted Josephson junctions [31–34] could be understood by carefully considering the role of non-zero temperature, finite-size, or non-perturbative effects [35].

Viewed from the broader perspective of response functions near quantum criticality, we have demonstrated a rare example where the thermal fluctuations with timescale  $\tau = \hbar/k_B T$  can be quantitatively traced through to experimentally measured resistance [13]. This does not result in an effectively Planckian scattering [24], as was recently observed in a different superconductor-insulator system [36]. It is also interesting to note that our saturating specific resistance curves empirically bear a strong resemblance to the anomalous-metallic phase in two-dimensional systems [22]. In our case, saturation is understood as a crossover effect towards insulating behavior. It would be interesting to perform a similar experimental program on a known anomalous-metallic system to test if saturation can be understood as a similar crossover effect.

## ACKNOWLEDGMENTS

We thank David Haviland, Jukka Pekola, Anton Babis and Alexander Shnirman for helpful feedback on the manuscript. This research was supported by the Scientific Service Units of IST Austria through resources provided by the MIBA Machine Shop and the Nanofabrication Facility. Work funded by Austrian FWF grant P33692-N. J.S. acknowledges funding from the European Union’s Horizon 2020 research and innovation program under the Marie Skłodowska-Curie Grant Agreement No. 754411.

## SUPPLEMENTARY MATERIALS

Raw data for all figures to be uploaded before final publication  
Materials and Methods  
Supplementary Text  
Figs. S1 to S15  
References [2, 13, 15, 23, 36–45]

\* Equal contribution

† [andrew.higginbotham@ist.ac.at](mailto:andrew.higginbotham@ist.ac.at)

- [1] S. Sachdev and B. Keimer, Quantum criticality, *Physics Today* **64**, 29 (2011).
- [2] S. L. Sondhi, S. M. Girvin, J. P. Carini, and D. Shahar, Continuous quantum phase transitions, *Rev. Mod. Phys.* **69**, 315 (1997).
- [3] R. M. Bradley and S. Doniach, Quantum fluctuations in chains of Josephson junctions, *Phys. Rev. B* **30**, 1138 (1984).
- [4] S. E. Korshunov, Effect of dissipation on the low-temperature properties of a tunnel-junction chain, *Sov. Phys. JETP* **68**, 609 (1989).
- [5] P. A. Bobbert, R. Fazio, G. Schön, and G. T. Zimanyi, Phase transitions in dissipative Josephson chains, *Phys. Rev. B* **41**, 4009 (1990).
- [6] P. A. Bobbert, R. Fazio, G. Schön, and A. D. Zaikin, Phase transitions in dissipative Josephson chains: Monte Carlo results and response functions, *Phys. Rev. B* **45**, 2294 (1992).
- [7] L. I. Glazman and A. I. Larkin, New quantum phase in a one-dimensional Josephson array, *Phys. Rev. Lett.* **79**, 3736 (1997).
- [8] M.-S. Choi, J. Yi, M. Y. Choi, J. Choi, and S.-I. Lee, Quantum phase transitions in Josephson-junction chains, *Phys. Rev. B* **57**, R716 (1998).
- [9] R. Fazio, K.-H. Wagenblast, C. Winkelholz, and G. Schön, Tunneling into one-dimensional Josephson chains and Luttinger liquids, *Physica B: Condensed Matter* **222**, 364 (1996), proceedings of the ICTP Workshop on Josephson Junction Arrays.
- [10] E. Chow, P. Delsing, and D. B. Haviland, Length-scale dependence of the superconductor-to-insulator quantum phase transition in one dimension, *Phys. Rev. Lett.* **81**, 204 (1998).
- [11] D. B. Haviland, K. Andersson, and P. Ågren, Superconducting and insulating behavior in one-dimensional Josephson junction arrays, *Journal of Low Temperature Physics* **118**, 733 (2000).
- [12] R. Fazio and H. van der Zant, Quantum phase transitions and vortex dynamics in superconducting networks, *Physics Reports* **355**, 235 (2001).
- [13] M. Bard, I. V. Protopopov, I. V. Gornyi, A. Shnirman, and A. D. Mirlin, Superconductor-insulator transition in disordered Josephson-junction chains, *Phys. Rev. B* **96**, 064514 (2017).
- [14] N. Vogt, R. Schäfer, H. Rotzinger, W. Cui, A. Fiebig, A. Shnirman, and A. V. Ustinov, One-dimensional Josephson junction arrays: Lifting the Coulomb blockade by depinning, *Phys. Rev. B* **92**, 045435 (2015).
- [15] K. Cedergren, R. Ackroyd, S. Kafanov, N. Vogt, A. Shnirman, and T. Duty, Insulating Josephson junction chains as pinned Luttinger liquids, *Phys. Rev. Lett.* **119**, 167701 (2017).
- [16] V. E. Manucharyan, J. Koch, L. I. Glazman, and M. H. Devoret, Fluxonium: Single Cooper-pair circuit free of charge offsets, *Science* **326**, 113 (2009).
- [17] N. A. Masluk, I. M. Pop, A. Kamal, Z. K. Mineev, and M. H. Devoret, Microwave characterization of Josephson junction arrays: Implementing a low loss superinductance, *Phys. Rev. Lett.* **109**, 137002 (2012).

- [18] L. B. Nguyen, Y.-H. Lin, A. Somoroff, R. Mencia, N. Grabon, and V. E. Manucharyan, High-coherence fluxonium qubit, *Phys. Rev. X* **9**, 041041 (2019).
- [19] I. V. Pechenezhskiy, R. A. Mencia, L. B. Nguyen, Y.-H. Lin, and V. E. Manucharyan, The superconducting quasicharge qubit, *Nature* **585**, 368 (2020).
- [20] N. Crescini, S. Cailleaux, W. Guichard, C. Naud, O. Buisson, K. Murch, and N. Roch, Evidence of dual shapiro steps in a josephson junctions array, arXiv:2207.09381 [10.48550/arXiv.2207.09381](https://arxiv.org/abs/10.48550/arXiv.2207.09381) (2022).
- [21] R. Kuzmin, R. Mencia, N. Grabon, N. Mehta, Y. H. Lin, and V. E. Manucharyan, Quantum electrodynamics of a superconductor–insulator phase transition, *Nature Physics* **15**, 930 (2019).
- [22] A. Kapitulnik, S. A. Kivelson, and B. Spivak, Colloquium: Anomalous metals: Failed superconductors, *Rev. Mod. Phys.* **91**, 011002 (2019).
- [23] T. Giamarchi and H. J. Schulz, Anderson localization and interactions in one-dimensional metals, *Phys. Rev. B* **37**, 325 (1988).
- [24] Supplementary materials.
- [25] At 150 mK the thermal length is more than an order of magnitude shorter than the device length.
- [26] Parameter uncertainties are propagated from systematic bands in Fig. 3, see Supplement [24].
- [27] M. Bard, I. V. Protopopov, and A. D. Mirlin, Decay of plasmonic waves in josephson junction chains, *Phys. Rev. B* **98**, 224513 (2018).
- [28] M. Houzet and L. I. Glazman, Microwave spectroscopy of a weakly pinned charge density wave in a superinductor, *Phys. Rev. Lett.* **122**, 237701 (2019).
- [29] H.-K. Wu and J. D. Sau, Theory of coherent phase modes in insulating josephson junction chains, *Phys. Rev. B* **99**, 214509 (2019).
- [30] P. Winkel, K. Borisov, L. Grünhaupt, D. Rieger, M. Spiecker, F. Valenti, A. V. Ustinov, W. Wernsdorfer, and I. M. Pop, Implementation of a transmon qubit using superconducting granular aluminum, *Phys. Rev. X* **10**, 031032 (2020).
- [31] R. Yagi, S.-i. Kobayashi, and Y. Ootuka, Phase diagram for superconductor-insulator transition in single small josephson junctions with shunt resistor, *Journal of the Physical Society of Japan* **66**, 3722 (1997).
- [32] J. S. Penttilä, U. Parts, P. J. Hakonen, M. A. Paalanen, and E. B. Sonin, “superconductor-insulator transition” in a single josephson junction, *Phys. Rev. Lett.* **82**, 1004 (1999).
- [33] L. S. Kuzmin, Y. V. Nazarov, D. B. Haviland, P. Delsing, and T. Claeson, Coulomb blockade and incoherent tunneling of cooper pairs in ultrasmall junctions affected by strong quantum fluctuations, *Phys. Rev. Lett.* **67**, 1161 (1991).
- [34] A. Murani, N. Bourlet, H. le Sueur, F. Portier, C. Altimiras, D. Esteve, H. Grabert, J. Stockburger, J. Ankerhold, and P. Joyez, Absence of a dissipative quantum phase transition in josephson junctions, *Phys. Rev. X* **10**, 021003 (2020).
- [35] K. Masuki, H. Sudo, M. Oshikawa, and Y. Ashida, Absence versus presence of dissipative quantum phase transition in josephson junctions, *Phys. Rev. Lett.* **129**, 087001 (2022).
- [36] C. Yang, H. Liu, Y. Liu, J. Wang, D. Qiu, S. Wang, Y. Wang, Q. He, X. Li, P. Li, Y. Tang, J. Wang, X. C. Xie, J. M. Valles, J. Xiong, and Y. Li, Signatures of a strange metal in a bosonic system, *Nature* **601**, 205 (2022).
- [37] V. Ambegaokar and A. Baratoff, Tunneling between superconductors, *Phys. Rev. Lett.* **10**, 486 (1963).
- [38] A. Kerr, S.-K. Pan, A. Lichtenberger, and D. Lea, Progress on tunerless sis mixers for the 200-300 ghz band, *IEEE Microwave and Guided Wave Letters* **2**, 454 (1992).
- [39] J. A. N. Bruin, H. Sakai, R. S. Perry, and A. P. Mackenzie, Similarity of scattering rates in metals showing  $T$ -linear resistivity, *Science* **339**, 804 (2013).
- [40] A. Legros, S. Benhabib, W. Tabis, F. Laliberté, M. Dion, M. Lizaire, B. Vignolle, D. Vignolles, H. Raffy, Z. Z. Li, P. Auban-Senzier, N. Doiron-Leyraud, P. Fournier, D. Colson, L. Taillefer, and C. Proust, Universal  $T$ -linear resistivity and planckian dissipation in overdoped cuprates, *Nature Physics* **15**, 142 (2019).
- [41] Y. Cao, D. Chowdhury, D. Rodan-Legrain, O. Rubies-Bigorda, K. Watanabe, T. Taniguchi, T. Senthil, and P. Jarillo-Herrero, Strange metal in magic-angle graphene with near planckian dissipation, *Phys. Rev. Lett.* **124**, 076801 (2020).
- [42] G. Grissonnanche, Y. Fang, A. Legros, S. Verret, F. Laliberté, C. Collignon, J. Zhou, D. Graf, P. A. Goddard, L. Taillefer, and B. J. Ramshaw, Linear-in temperature resistivity from an isotropic planckian scattering rate, *Nature* **595**, 667 (2021).
- [43] A. Jaoui, I. Das, G. Di Battista, J. Díez-Mérida, X. Lu, K. Watanabe, T. Taniguchi, H. Ishizuka, L. Levitov, and D. K. Efetov, Quantum critical behaviour in magic-angle twisted bilayer graphene, *Nature Physics* **18**, 633 (2022).
- [44] J. P. Pekola, K. P. Hirvi, J. P. Kauppinen, and M. A. Paalanen, Thermometry by arrays of tunnel junctions, *Phys. Rev. Lett.* **73**, 2903 (1994).
- [45] K. P. Hirvi, J. P. Kauppinen, A. N. Korotkov, M. A. Paalanen, and J. P. Pekola, Arrays of normal metal tunnel junctions in weak coulomb blockade regime, *Applied Physics Letters* **67**, 2096 (1995).

# Superconductivity from a melted insulator

S. Mukhopadhyay,<sup>1,\*</sup> J. Senior,<sup>1,\*</sup> J. Saez-Mollejo,<sup>1</sup> D. Puglia,<sup>1</sup> M. Zemlicka,<sup>1</sup> J. Fink,<sup>1</sup> and A.P. Higginbotham<sup>1,†</sup>

<sup>1</sup>*IST Austria, Am Campus 1, 3400 Klosterneuburg, Austria*

## CONTENTS

I. Extraction of chain parameters	2
A. Josephson energy interpolation	3
B. Chain and junction parameters	3
II. Schematic of the chip	5
III. Device setup and connections	6
IV. Nanofabrication	8
V. Current-peak spacings	8
VI. Base electron temperature	9
VII. Comparing energy scales	10
VIII. Systematics in measurement/analysis	11
A. Heating	11
B. Upturn	12
C. Voltage Offsets	13
D. Power law fits	14
E. Global superfluid stiffness	15
IX. Additional analysis	16
A. Scaling	16
B. Planckian limit	17
X. Theory	18
A. Boundaries in theoretical phase diagram	18

---

\* Equal contribution

† [andrew.higginbotham@ist.ac.at](mailto:andrew.higginbotham@ist.ac.at)

# I. EXTRACTION OF CHAIN PARAMETERS

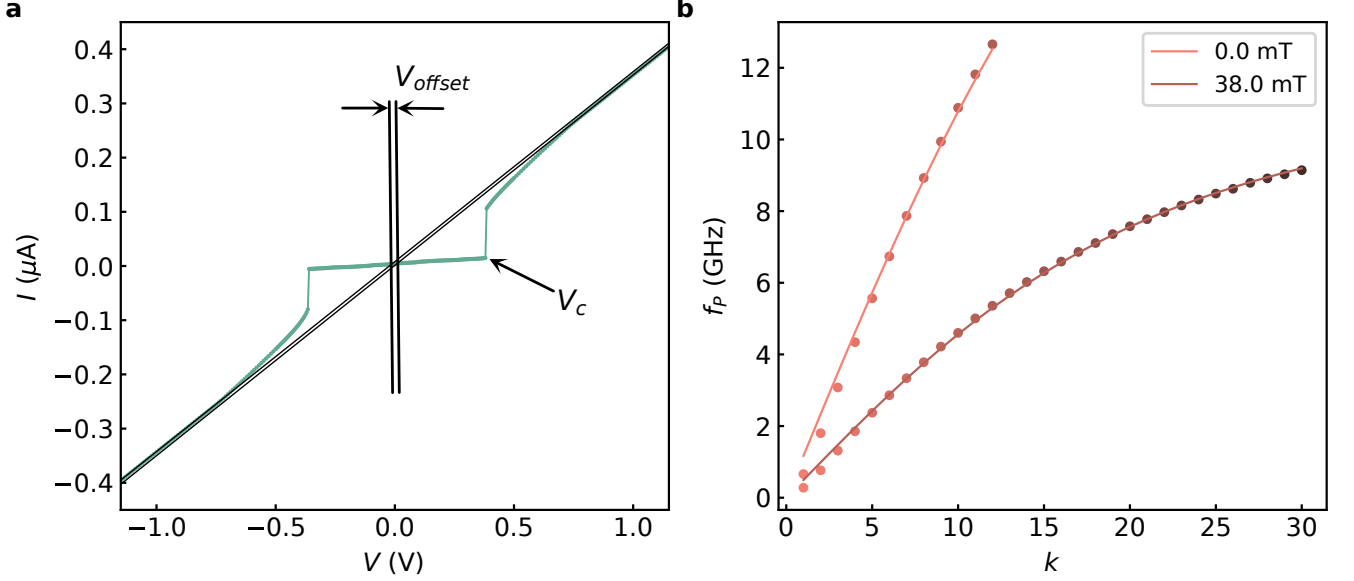


**Figure S1: Extraction of chain parameters  $E_C, E_J, E_g$ .** **a**, Measured current  $I$  versus applied voltage  $V$ . Linear fits to the high bias features extract  $E_C, E_J$ .  $V_c$  is the critical voltage. **b**, Extracted resonant peak frequency  $f_P$  versus mode number  $k$ . The curves are fit from the dispersion relation, which yields  $E_g$ , and  $E_J$  as a function of magnetic field.

In the transport device, a voltage offset  $V_{\text{offset}}$  is extracted by extrapolating the linear parts of the current-voltage characteristic down to zero bias (Fig. S1a).  $E_C$  is then inferred from  $V_{\text{offset}}$  using [15]

$$E_C = 4eV_{\text{offset}}/N, \quad (\text{S1})$$

which gives the value quoted in the main text.

Once  $E_C$  is fixed from transport, microwave measurements are used to determine  $E_g$  and  $E_J(B)$ . The dispersion relation for plasma-mode resonant frequency  $f_{P,k}$  is

$$f_{P,k} = \omega(k)/\sqrt{1 + (\omega(k)/\omega_p)^2}, \quad (\text{S2})$$

where  $\omega_p = \sqrt{2E_J E_C}$  and  $\omega(k) = \pi k \sqrt{2E_J E_g}/N$ , with  $N$  being the number of junctions. Fitting Eq. S2 to the experimental data, as in Fig. S1b, yields  $E_g$  and  $E_J(B)$ . Sample values determined with this method are presented in Fig. S2 and Table SII.

Two independent checks are available on the extracted system parameters. The charging energy  $E_C$  can be estimated from geometry and the nominal specific capacitance of our Josephson junctions. Josephson energy can be estimated with the Ambegaokar-Baratoff relation [37]

$$E_J = N\Delta h/(8e^2 R_N), \quad (\text{S3})$$

where  $N$  is the number of junctions and  $\Delta$  is the superconducting gap of Aluminum. These independent checks on  $E_C$  and  $E_J$  are shown in Table SIII.



### A. Josephson energy interpolation

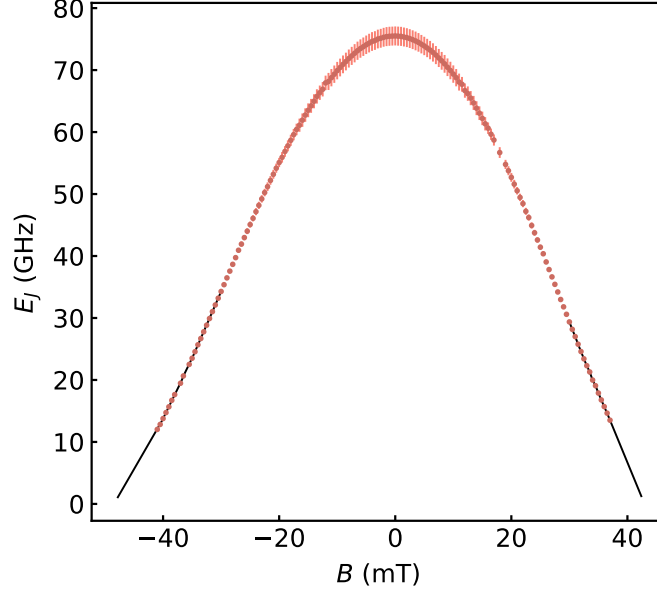


**Figure S2:  $E_J(B)$  interpolation.** Josephson energy  $E_J$ , determined from fitting dispersion curves, as a function of the magnetic field  $B$ . Error bars are the standard error resulting from the fits. Black lines represent a linear interpolating function used at higher magnetic fields used to estimate  $B^{\text{ins}}$ , see Sec. VII for further details.

The field-driven superconductor-insulator transition in our system is expected to occur at a magnetic field  $B^{\text{ins}}$ . As discussed in Sec. VII,  $B^{\text{ins}}$  is determined by numerically solving  $\pi K_c(B^{\text{ins}}) = 1$ . To accomplish this we interpolate  $E_J(B)$  linearly out to  $B^{\text{ins}}$ , which is justified by the smooth, linear behavior observed in  $E_J$  over similar field ranges, as shown in Fig. S2.

### B. Chain and junction parameters

Parameter	Notation	Microwave	Transport
Number of junctions	$N$	1227	1217
Chain length	$L$	912 $\mu\text{m}$	905 $\mu\text{m}$
Junction Area	$A$	0.28 $\pm$ 0.01 $\mu\text{m}^2$	

**Table SI: Chain and junction geometry.** Chain length and number of junctions refer to the designed values. Geometry of a junction (or the chain) is estimated from SEM imaging. For details refer to section *Nanofabrication*.

The error in  $A$  is the propagated error from estimating length and breadth of a single junction from a SEM image.

Parameter (@ $B = 0$ T)	Notation	Value	Method
Charging energy	$E_C/h$	5.11 $\pm$ 0.04 GHz	Eq. S1
Charging energy to ground	$E_g/h$	1390 $\pm$ 40 GHz	Fig. S1b
Josephson energy	$E_J/h$	75.5 $\pm$ 1.5 GHz	Fig. S1b
Normal state resistance of chain	$R_N$	2857.11 $\pm$ 0.08 k $\Omega$	Fig. S1a
Critical voltage of chain	$V_c$	0.374 $\pm$ 0.001 V	Fig. S1a

**Table SII: Extracted parameters.** For calculations discussed in text,  $E_J$  and  $E_g$  inferred from microwave measurements are used, whereas  $E_C$  inferred from transport measurements are used.

The error in  $E_g$  is the standard error in the values of  $E_g$  inferred from fits to the dispersion curves at high magnetic

fields. The error in  $E_J$  is the standard error from fit to the dispersion curve at  $B = 0$  T. The error in  $E_C$ ,  $R_N$  and  $V_c$  is the difference between charging energies, high-bias resistances and critical voltages inferred from up and down I-V sweeps.

The following table serves as a cross-check of the junction parameters mentioned in Table SII above:

Parameter	Value	Method
Charging energy	$6.1 \pm 0.2$ GHz	$(2e)^2/(2C_s \times A)/h$
Josephson energy	$54.73 \pm 0.06$ GHz	Eq. S3

**Table SIII: Independent checks on extracted parameters.** Empirical specific capacitance of a junction  $C_s = 45$  fF/ $\mu\text{m}^2$  [38]. Superconducting gap of bulk Aluminum,  $\Delta = 180$   $\mu\text{eV}$ .

The errors in the parameters of Table SIII are propagated from the errors in  $A$  (Table SI) and  $R_N$  (Table SII). Table SIV contains a list of chain/junction parameters that have been derived from the measured values presented in Table SII:

Parameter (@ $B = 0$ T)	Notation	Value	Formula
Junction capacitance	$C_c$	$15.1 \pm 0.1$ fF	$(2e)^2/(2E_C)$
Junction capacitance to ground	$C_g$	$55.9 \pm 1.5$ aF	$(2e)^2/(2E_g)$
Junction inductance	$L_J$	$42.7 \pm 0.8$ nH	$(h/2e)^2/(2E_J)$
Impedance	$Z$	$27.6 \pm 0.6$ k $\Omega$	$\sqrt{L_J/C_g}$
Local superfluid stiffness	$K_C$	$2.72 \pm 0.04$	$\sqrt{E_J/2E_C}$
Global superfluid stiffness	$K_g$	$0.165 \pm 0.003$	$\sqrt{E_J/2E_g}$
Plasma frequency	$\omega_p$	$27.7 \pm 0.3$ GHz	$\sqrt{2E_J E_C}/h$
Charge screening length	$\Lambda$	$16.4 \pm 0.2$	$\sqrt{E_g/E_C}$
Bloch bandwidth	$W$	$149 \pm 3$ Hz	Eq. S4

**Table SIV:** Chain/junction parameters inferred from Table SII.

$$W = 16(E_J E_C / \pi)^{1/2} (2E_J / E_C)^{1/4} e^{-\sqrt{32E_J/E_C}}. \quad (\text{S4})$$

The errors for each parameter in Table SIV are propagated from corresponding errors in the parameters mentioned in Table SII.

## II. SCHEMATIC OF THE CHIP

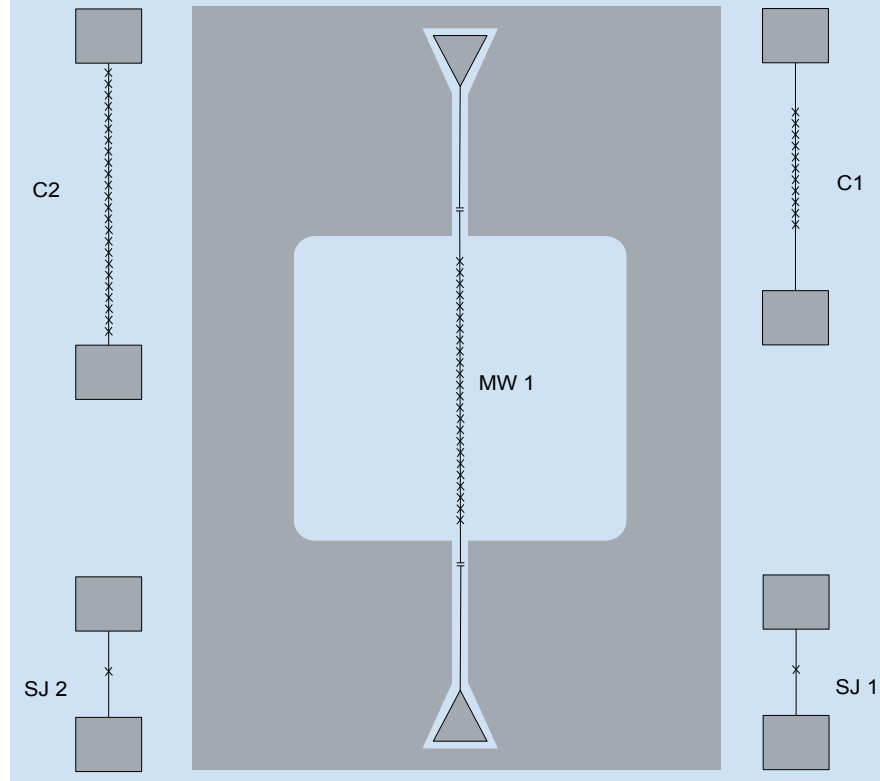


**Figure S3: Schematic of the nanofabricated chip.** Blue background represents Silicon. Grey represents Aluminum. Each cross represents a single Josephson junction.

MW1 refers to the chain of Josephson junctions capacitively coupled on either side to  $50\ \Omega$  microwave launchers. C1 and C2 refer to transport chains. C2 contains nominally the same number of junctions as on the microwave chain, MW1. C1 has half as many junctions as C2. SJ1 and SJ2 are identical single junction transport devices, with the same junction geometry as on the microwave and transport chain devices. Ground plane around the array of junctions of the microwave device (MW1) has been removed with the intention of decreasing capacitance to ground.

### III. DEVICE SETUP AND CONNECTIONS

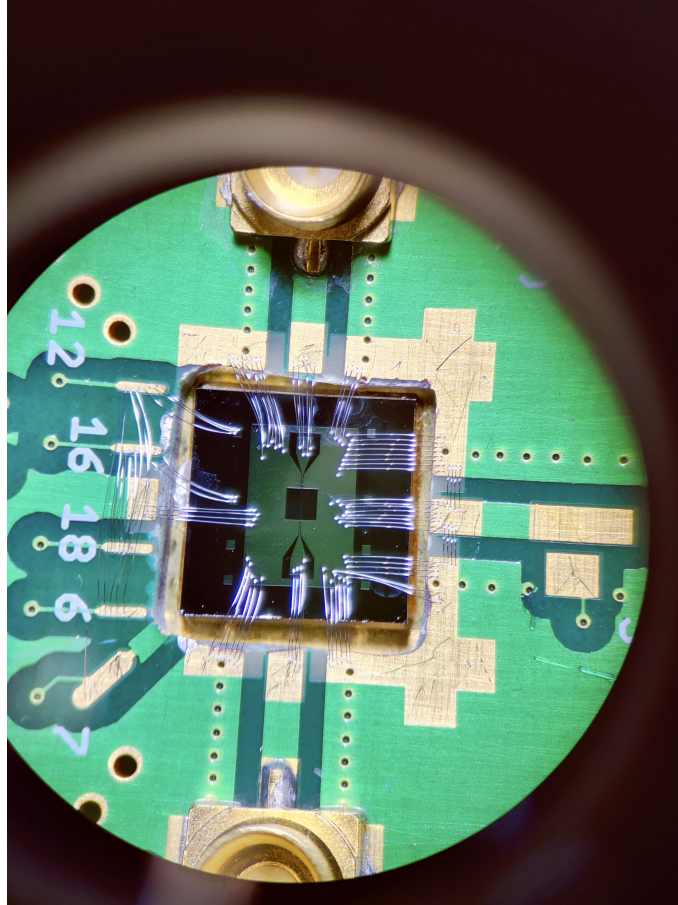


**Figure S4: Chip bonded onto PCB.** Numbers on the PCB indicate connections to DC lines for four/two probe transport measurements. SMP launchers for microwave connections can be seen partially at the top and bottom of the picture.

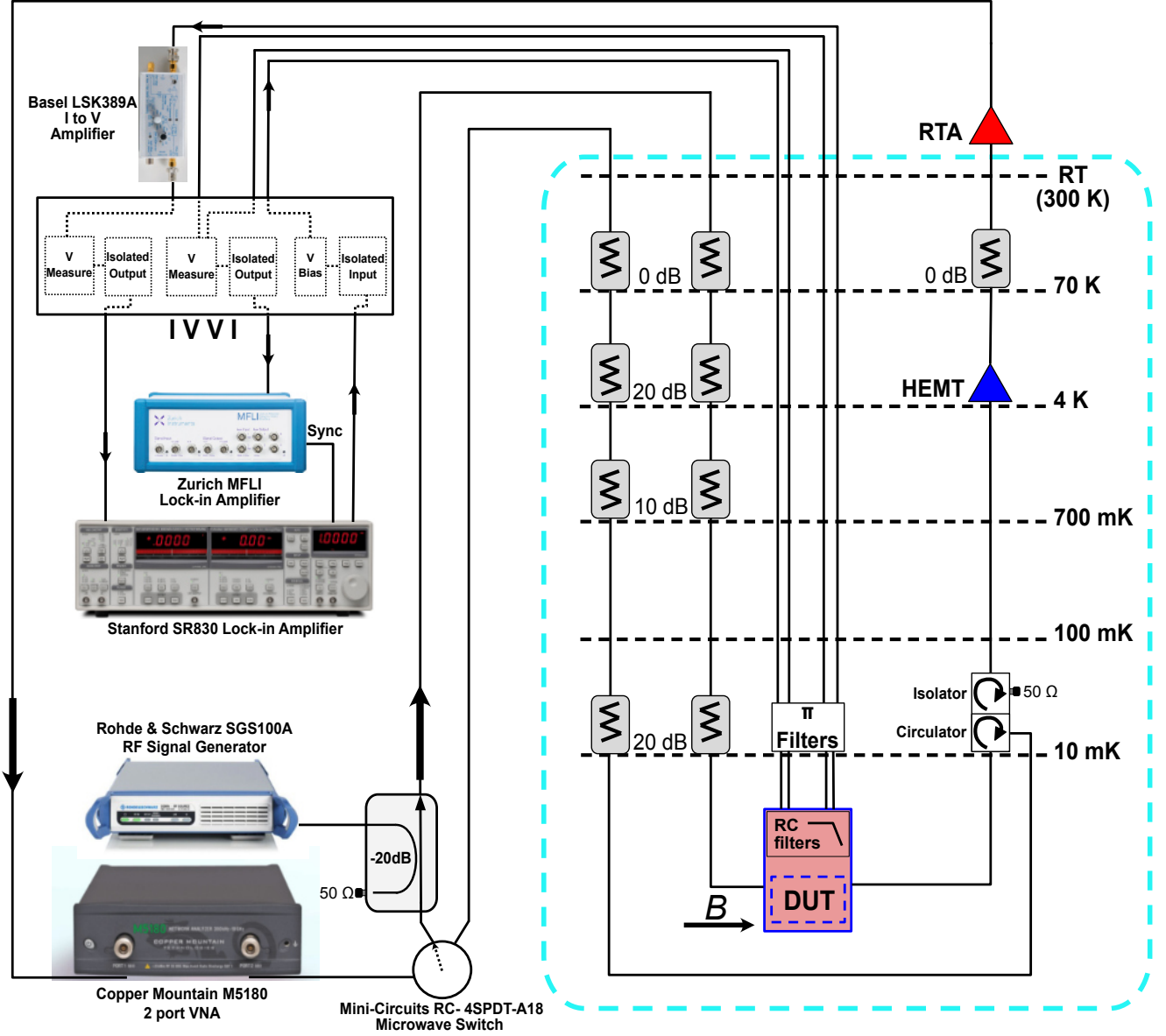


**Figure S5: The experimental setup.** The Dilution Fridge represented as cyan colored dashed boundary. The signal generator is coupled to the output port of the VNA through a RF coupler which has a 20 dB insertion loss at the coupled port. The ‘resistor’ symbol at each stage of the fridge represent the installed microwave cryogenic attenuators. ‘RTA’ refers to Room Temperature Amplifier with a gain of around 35 dB. ‘HEMT’ refers to High-Electron-Mobility-Transistor, which is the Low Noise Amplifier (noise  $\sim 2$  K) with a gain of around 36 dB at 4 K. ‘DUT’ refers to ‘Device Under Test’. ‘B’ indicates the direction of applied external magnetic field.

Microwave measurements are done in transmission, where the output (amplifier) line has double junction isolator attached to the mixing chamber stage of the dilution fridge. In addition, the output line has LNF HEMT attached to the 4 K stage and another LNF amplifier attached to the room temperature stage of the cryostat. The input line has 50 dB of net attenuation with 0 dB at 70 K stage, 20 dB at 4 K stage, 10 dB at 700 mK stage and 20 dB at mixing chamber stage of the cryostat.

The DC lines are equipped with three cascaded LFCN filter boards attached to the mixing chamber stage of the dilution fridge; each filter board provides cut-off at different frequencies. The three cut-off frequency ranges are (DC – 5000 MHz), (DC – 1450 MHz) and (DC – 80 MHz). Each board has filters soldered onto them in six stages for all the DC lines. The PCB onto which the chip is bonded, has single stage low pass filtering (2 k $\Omega$  ; 47 nF) for each DC line. So, in all each DC line has nineteen stage low-pass filtering at the mixing chamber stage of the cryostat.



#### IV. NANOFABRICATION

- The chains were fabricated on a high resistivity Silicon substrate ( $> 10^4 \Omega\text{cm}$ ), which was diced into  $7 \times 7 \text{ mm}$  chips, ultrasonicated in Acetone (2 min / power 4) and then in IPA (2 min / power 4).
- The chips were baked at 170 C for 3 mins before spin coating with MMA (EL-13), followed by PMMA (950k 4%). Spin coating recipe was developed such that thickness of MMA is 670 nm and of PMMA is 290 nm. The chips were again baked at 170 C for 3 mins after each spin coating step.
- Standard e-beam lithography was done in Raith EBPG5150, after which the pattern was developed in IPA : water (3 : 1) solution for 90 secs.
- The developed chip was then subjected to electron beam evaporation with Aluminum, in a double angle shadow evaporation process in Plassys UHV MEB550S2, with an intermediate in-situ static oxidation step (5 mbar/5 mins). The evaporation was terminated with another in-situ static oxidation step (10 mbar/2 mins). Before evaporating Aluminum, the evaporation chamber was gettered with Titanium for 3 mins at 0.2 nm/sec to further bring down the pressure of the chamber. In the first evaporation step, 60 nm of Aluminum was deposited, whereas on the second step 120 nm of Aluminum was deposited; with an evaporation rate of 1 nm/sec in both steps.
- Lift-off was done using hot NMP (80 C) for 45 mins, after which the chip was successively cleaned in cold NMP, Acetone and IPA.
- SEM imaging of the JJ chain revealed the junction (or chain) width  $\sim 510 \text{ nm}$ , and the junction overlap  $\sim 560 \text{ nm}$ .

#### V. CURRENT-PEAK SPACINGS

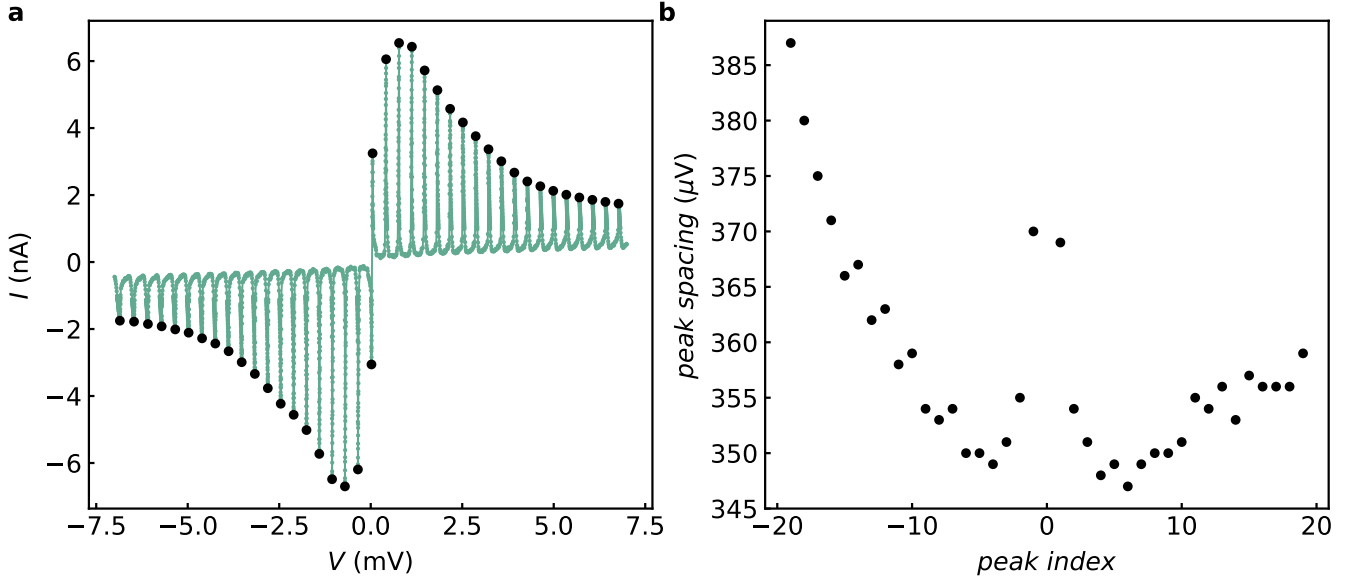


**Figure S6: Peak extraction and spacings.** **a**, Measured current  $I$  versus applied voltage  $V$ . The black dots represent detected current peaks. **b**, Peak spacings versus the peak index. Each peak index refer to the succeeding peak spacing on positive bias and to the preceding peak spacing on negative bias.

The typical peak spacing is comparable to twice the superconducting gap of Aluminum,  $360 \mu\text{eV}$ . There is an overall smooth evolution of the peak spacings which is asymmetric in bias, which is not understood (Fig. S6b). Peak spacings are enhanced around zero bias, which we speculate is due to an interaction effect. Namely, the weakest link in the chain is the one which, due to offset charge disorder, is in the deepest Coulomb blockade. This link should switch first, and then require increased bias before current can flow. This picture predicts a that peak spacings should increase near zero bias, as we consistently observe.

## VI. BASE ELECTRON TEMPERATURE

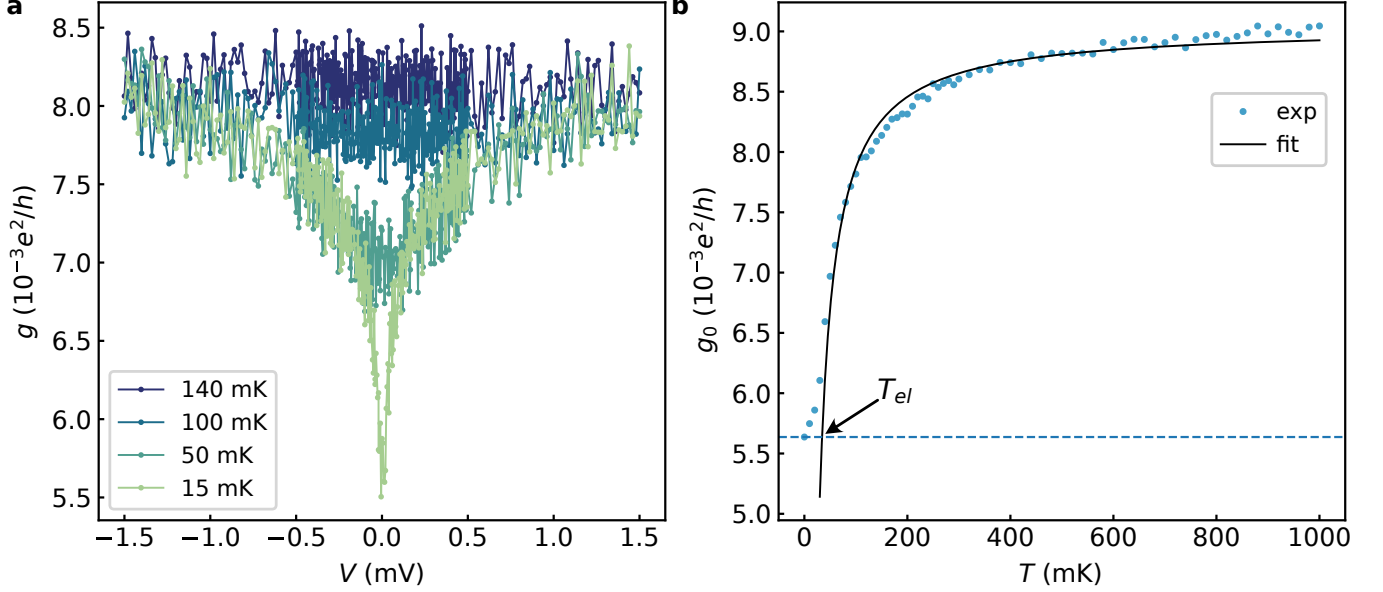


**Figure S7: Coulomb Blockade Thermometry at large magnetic fields.** **a**, Differential conductance  $g$  versus the applied voltage  $V$ , at various setpoint temperatures. **b**, Zero bias differential conductance  $g_0$  versus the setpoint temperature  $T$ . Black line is a function fit to the data. The dashed blue line is the  $g_0$  value corresponding to the lowest data point.  $T_{el}$  is the inferred base electron temperature of the system. Data in this figure is taken with the JJ chain being in normal state, at 500 mT.

Coulomb-blockade thermometry is performed in the normal state by applying a large, perpendicular magnetic field. Measuring differential conductance versus applied voltage shows a sharp dip at zero bias, which gets shallower on raising the temperature of the system (Fig. S7a). Extracting the zero bias differential conductance  $g_0$  at all setpoint temperatures, shows a gradual decline in conductance below 400 mK, and a sharp fall below 100 mK (Fig. S7b).  $g_0$  is fit to the well-known expression for Coulomb blockade thermometry [44, 45]

$$g_0 = g_T(1 - ((N - 1)/N)E_C/(3k_B T)), \quad (S5)$$

where  $g_T$  is the asymptotic  $g$  at high bias voltages,  $N$  is the number of junctions in the chain and  $E_C$  is the charging energy of a junction. At high temperature the data agree well with Eq. S5. At low temperature the conductance is larger than the expected value, indicating that the device falls out of equilibrium with the cryostat. Associating the smallest observed conductance with a temperature gives the base electron temperature  $T_{el} = 35$  mK.

## VII. COMPARING ENERGY SCALES

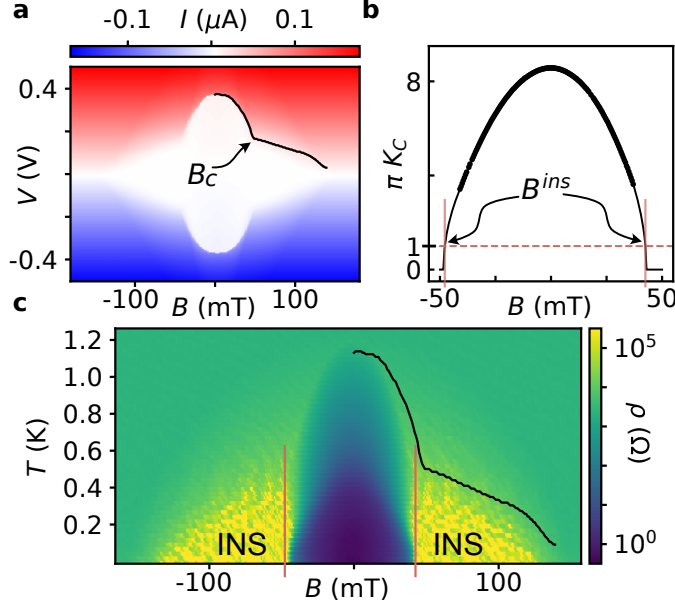


**Figure S8: Overlay of energy scales on the phase diagram.** **a**, Measured current  $I$  versus the bias voltage  $V$  and magnetic field  $B$ . The black curve indicates extracted critical voltage  $V_c$ . Kink in  $V_c$  at critical field  $B_c$  indicated. **b**, Inferred local superfluid stiffness  $\pi K_C$  versus the magnetic field  $B$ . Black dots are the inferred stiffness from experimental data. Solid black line is based on a linear extrapolation of  $E_J(B)$  down to  $E_J \rightarrow 0$ , which is justified by the empirical observation that  $E_J$  is linear at high fields.  $B^{\text{ins}}$  is defined implicitly by  $\pi K_C(B^{\text{ins}}) = 1$ . **c**, The phase diagram with the zero bias differential specific resistance  $\rho$  as a function of the magnetic field  $B$  and temperature  $T$ . INS refers to Insulator. The black curve is the edge feature extracted from **a**, scaled by an empirical proportionality constant of  $1/(N2\pi k_B)$ . The vertical red lines in **b** and **c** correspond to the field values  $|B| = B^{\text{ins}}$ . Note that,  $|B^{\text{ins}}| < |B_c|$ .

In the main text, we discussed that the wide-range current-voltage characteristic exhibits strongly suppressed current for biases below the critical voltage  $V_c$  (Fig. 1b and Fig. S1a). This voltage roughly corresponds to the value for biasing  $N$  junctions by  $2\Delta/e$  such that current can flow in the voltage state.

Examining the field dependence of this current-voltage characteristic yields further information on the evolution of  $\Delta$ . Measuring current while varying bias voltage and magnetic field (Fig. S8a) reveals that  $V_c$  has a smooth field dependence up to a critical field value of  $B_c = 49$  mT, at which point it exhibits a kink. The kink is most likely due to the critical field of the thicker islands in the Josephson array; this is expected critical field for a 120 nm Al film thickness, and also naturally explains why the kink occurs at approximately  $V_c(B=0)/2$ . Importantly, this critical field exceeds the field at which insulating behavior is observed  $B_c > B^{\text{ins}}$ , so all islands are superconducting when the array transitions to insulating behavior.

The expected value of  $B^{\text{ins}}$  is found from the criteria  $\pi K_C(B^{\text{ins}}) = 1$  (Fig. S8b), yielding a value  $B^{\text{ins}} = 42.5$  mT at positive field and  $B^{\text{ins}} = -47.8$  mT at negative field. Since  $B^{\text{ins}}$  lies slightly beyond the range where microwave measurements are possible, we have performed a linear extrapolation of  $E_J(B)$  down to the regime  $E_J \rightarrow 0$ , justified by the linear behavior of  $E_J$  over a wide field range. The observed field-asymmetry in  $B^{\text{ins}}$  reflects the fact that the magnetic-field dependence of the microwave is not perfectly field-symmetric, which is not understood. A consistent field-asymmetry is also present in the transport phase diagram, where the transition to the insulating state is also slightly field-asymmetric. We also note again that  $|B_c| > |B^{\text{ins}}|$ .

As shown in Fig. S8c and also discussed in the main text, the theoretical value of  $B^{\text{ins}}$  matches the experimentally observed transition to insulating behavior. It is also interesting to note that the overall dependence of  $V_c(B)$  qualitatively matches the dome and wing structure of the phase diagram (Fig. S8c, black line).

## VIII. SYSTEMATICS IN MEASUREMENT/ANALYSIS

The zero bias differential resistance of the transport JJ chain was measured using four probe lock-in setup. Stanford SR830 was used to measure the differential current  $dI$  through the chain, before which the current signal was converted to voltage using Basel LSK389A transimpedance amplifier. The differential voltage drop across the chain,  $dV$  was measured with a Zurich MFLI. A voltage amplitude of  $1 \mu\text{V}$  was applied, which we experimentally verified was sufficiently small to avoid overheating (see below). Throughout the main text, the two-probe resistance is plotted with the inferred line resistance from a four-probe measurement subtracted. This procedure removes technical noise at the expense of introducing a small (few Ohm) systematic error in the data.

### A. Heating

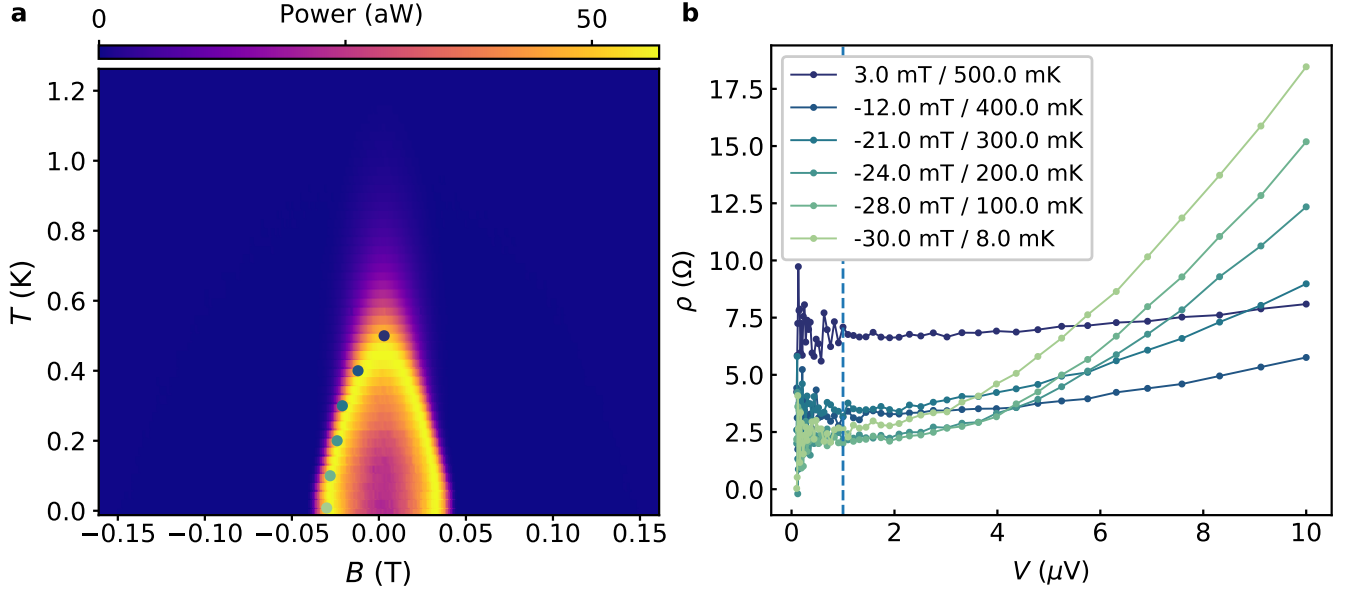


**Figure S9: Heat check for the transport JJ chain.** **a**, Power dissipated at the chain versus temperature  $T$  and magnetic field  $B$ . **b**, Zero bias differential specific resistance  $\rho$  versus lock-in voltage amplitude  $V$ : at various  $(B, T)$  points along the region of maximal power dissipation in **a**. The dashed line indicates the voltage ( $1 \mu\text{V}$ ) used for measuring the phase diagram.

Mapping out power dissipated ( $dI \times dV$ ) at the device over full  $(B, T)$  parameter space (Fig. S9a), reveals a dome-like feature of maximal power dissipation. Choosing a few points over the dome to do an amplitude study (Fig. S9b), reveals that the device lies comfortably in the linear response regime till  $2 \mu\text{V}$  of voltage amplitude.

## B. Upturn

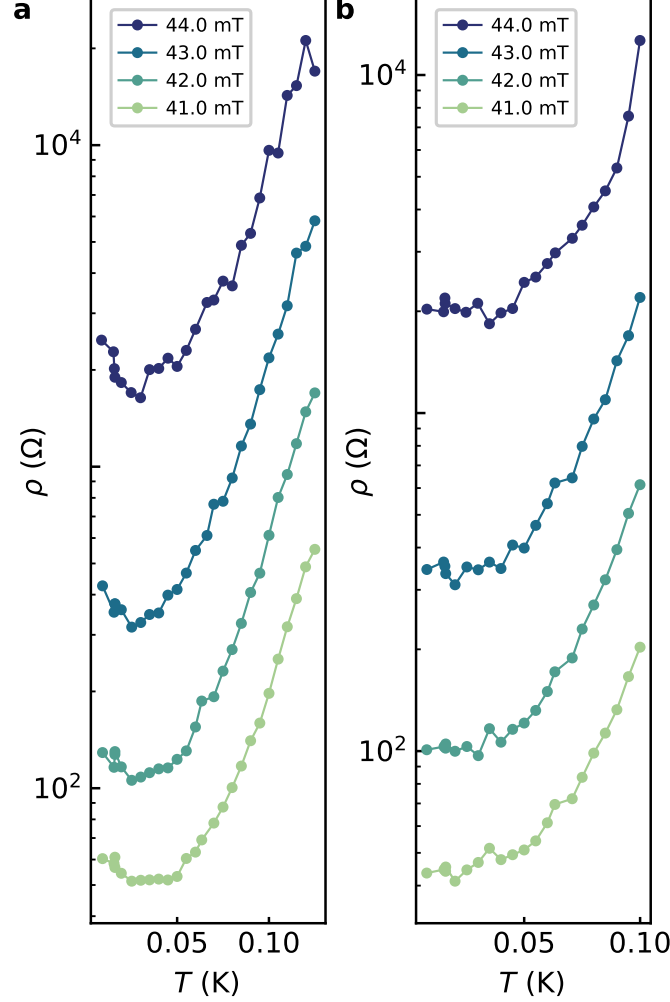


**Figure S10: Reproducibility of the upturn feature.** **a**, Zero-bias differential specific resistance  $\rho$  as a function of measured temperature  $T$ , at various magnetic fields. **b**, The same measurement repeated on a different run and same cooldown.

As pointed out in Fig. S10, a low-temperature upturn in resistance is inconsistently observed at fields slightly lower than the data in the main text. The upturn measurement is done at the boundary of LSC/INS phases (refer to Fig. 4c in main text), where on lowering temperature, the device resistance transitions from low to a very high value. Measuring extremely low currents at such phase boundary is challenging, owing to the highly fluctuating values of the locked-in signal. Two customizations were done in this regard:

- (a) Turning up the voltage amplitude to  $10 \mu\text{V}$ .
- (b) Measuring the  $dI$ ,  $dV$  over ten time points and recording the mean value.

To ensure that the device does not heat up on increasing the lock-in excitation, amplitude study (similar to one depicted in Fig. S9b) was done at temperature corresponding to the minimum resistance. At such regime, the device resistance is higher than the line resistance in the measurement chain, making the device effectively voltage biased. Hence, maximum heating is expected at the point of minimum resistance. However, the device maintained linear response in the amplitude study.



### C. Voltage Offsets

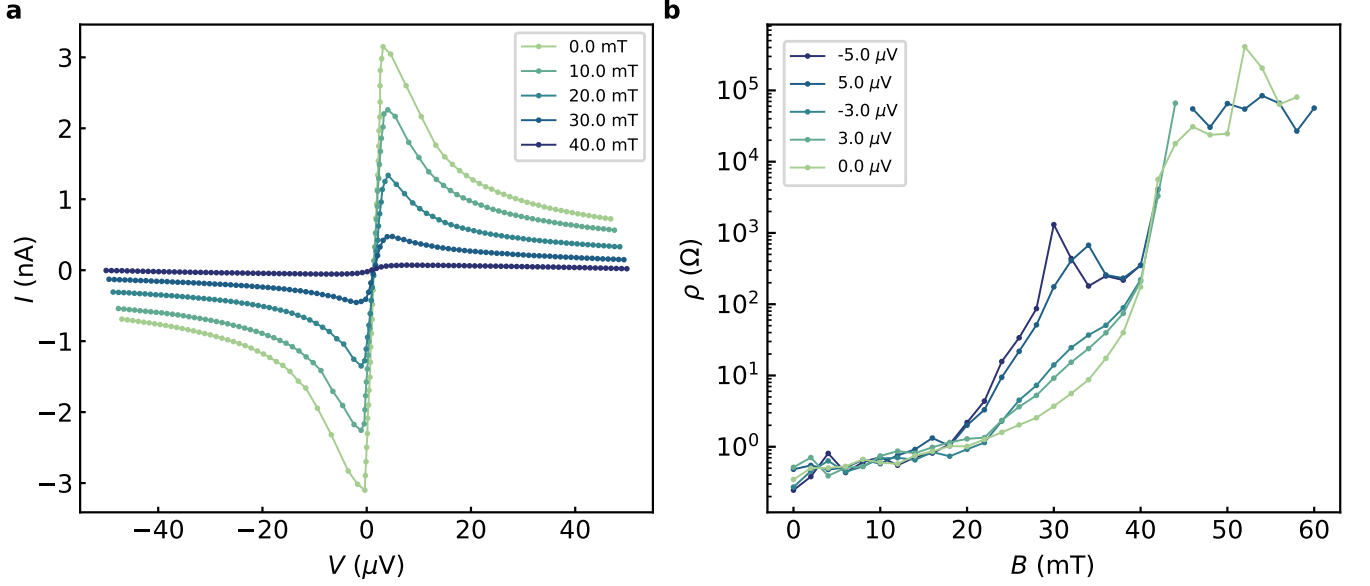


**Figure S11: Effect of voltage offsets in specific resistance measurement.** **a**, Current  $I$  versus the applied voltage  $V$ , in the narrow bias range, measured at various magnetic fields. **b**, Zero bias specific differential resistance  $\rho$  versus the magnetic field  $B$ , with and without applied offset voltages.

The supercurrent peak, and the zero bias conductance, gradually decreases on increasing the magnetic field (Fig. S11a). Lock-in setup measures the slope of the zero bias peak. As shown in Fig. S11b, adding voltage offsets to the lock-in measurement changes the behavior of the device in the region where the device transitions from LSC to INS phase (refer to Fig. 4c in main text). Hence, ensuring proper offset correction at zero voltage bias is essential to measurement of the phase diagram.

## D. Power law fits

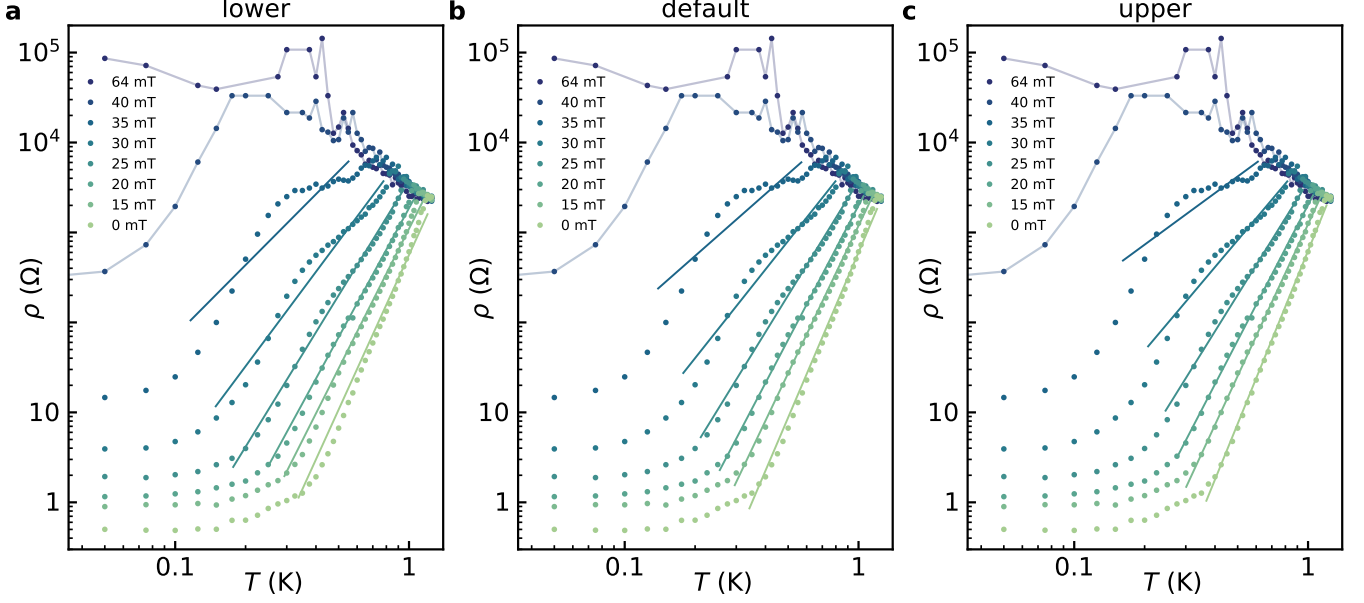


**Figure S12: Power law fits with various choices of lower cutoffs.** **a**, Zero bias specific differential resistance  $\rho$  versus temperature  $T$ , with  $0.18 T_P$  as the lower cutoff temperature for power law fits. **b**, Same plot with  $0.215 T_P$  as the lower cutoff temperature for fits. **c**, Same plot with  $0.25 T_P$  as the lower cutoff temperature for fits.  $T_P$  is the plasma frequency in temperature units.

To analyze the power-law behavior of  $\rho(T)$ , fits must be performed over a restricted temperature range. Because system parameters evolve with magnetic field, the fit range must also be field dependent. The high-temperature limit of the fitting range is chosen to be 95% of the plasma temperature  $T_P$ , where

$$T_P = \sqrt{2E_J(B)E_C}/k_B. \quad (\text{S6})$$

As shown in the main text, the upper edge of the local superconducting dome follows the plasma temperature, so this is a suitable upper bound.

The low-temperature limit of the fitting range is not as easy to sharply define, due to the smooth crossover to saturating resistance. To account for this difficulty, we explored a range of lower cutoff values, as shown in Fig. S12. These cutoff values are used to create the blue error bands for the exponent  $p$  in Fig. 3b of the main text. To evaluate the impact of the systematic error bands on fit parameters,  $p(K_c)$  was fit to a line for the three lower cutoffs in Fig. S12. The range of values obtained are reported as uncertainties in the slope and intercept in the main text.

### E. Global superfluid stiffness

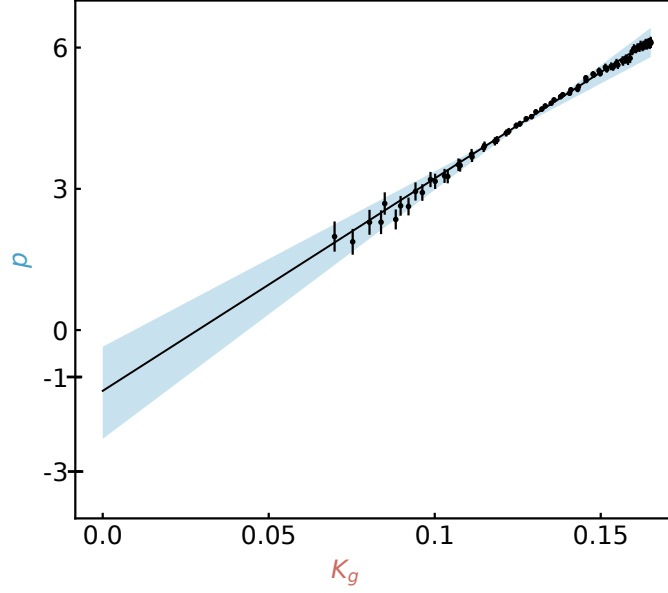


**Figure S13: Comparing the powers with global superfluid stiffness.** Exponent  $p$  from power-law fits versus the global superfluid stiffness  $K_g$  from microwave measurements. Solid line is a linear fit. Shaded blue region depicts the systematic error resulting from the choice of lower resistance cutoff in the power law fits.

Solving the Renormalization Group (RG) equations in the UV limit, yields a power law with exponent  $\pi K_C - 1$  (Eq. S10), where  $K_C$  is the bare value of  $K$  in RG flow. While solving in the IR limit, with renormalized  $K$ , results in a power law with exponent  $2\pi K_g - 3$ .

Comparing  $p$  from the transport measurements with the global superfluid stiffness  $K_g$  inferred from microwave measurements reveals a linear behavior (Fig. S13) with slope  $45 \pm 7$  and intercept of  $-1.3 \pm 1.0$ . This is in complete disagreement with the predicted slope of  $2\pi$  for global superconductivity. The intercept close to  $-1$  is same as observed for local superconductivity (Fig. 3b in main text), owing to the fact that only the x-axis is scaled down on plotting versus  $K_g$ .

## IX. ADDITIONAL ANALYSIS

### A. Scaling

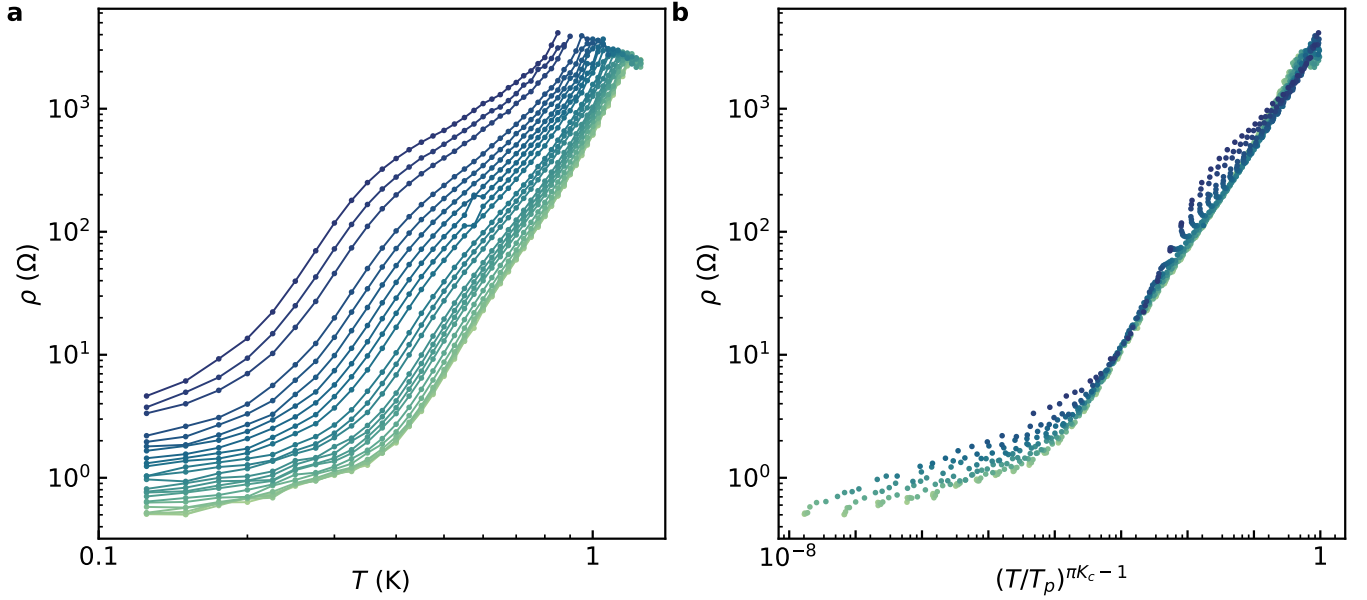


**Figure S14: Collapse of power laws.** **a**, Zero bias specific differential resistance  $\rho$  as a function of temperature  $T$ , at various magnetic fields. **b**, The same data in **a** plotted with scaled temperature axis, where  $T_P$  is the plasma frequency in temperature units and  $K_C$  is the local superfluid stiffness.

As shown in Fig. S14a, the power law behavior of specific resistance with temperature is observed until about 40 mT. In Fig. S14b, scaling the normalized temperature axis with expected exponent collapses all the data on left into an universal power law behavior, removing the field dependency of the data. As pointed out earlier in Eq. S6,  $T_P$  is a field dependent quantity.

## B. Planckian limit

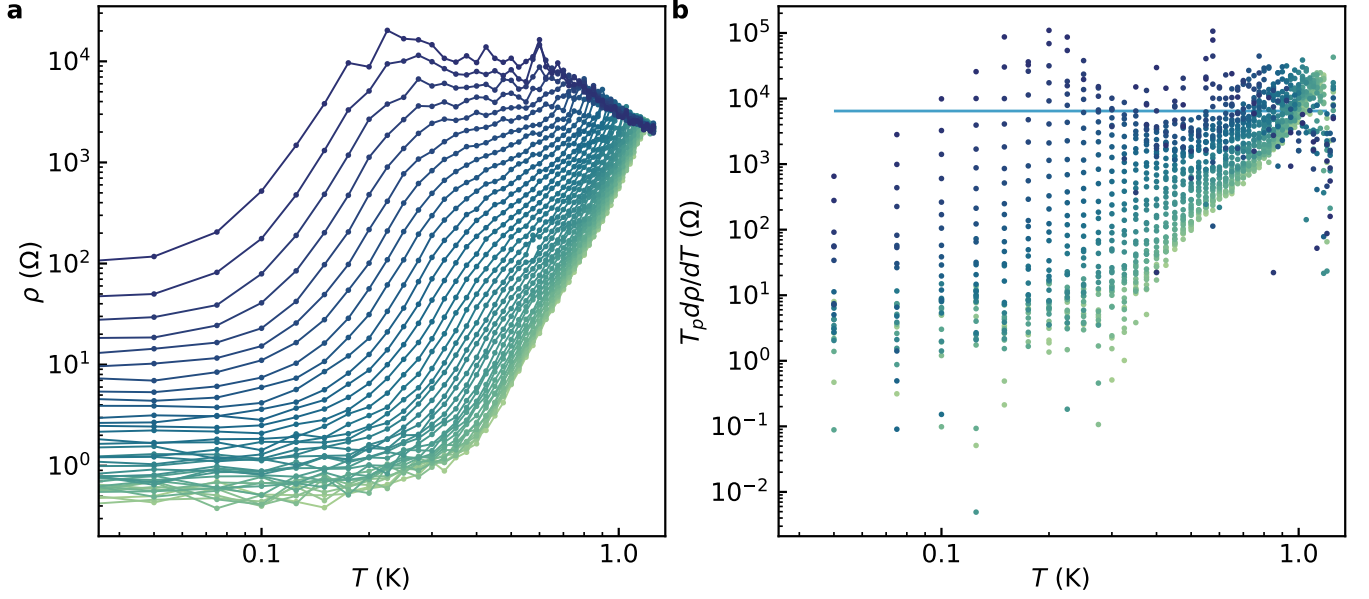


**Figure S15: Planckian slope check.** **a**, Zero bias specific differential resistance  $\rho$  as a function of temperature  $T$ , at various magnetic fields. **b**, The slope of the curves in **a**, times the plasma frequency  $T_P$ , versus temperature  $T$ . The blue horizontal line is the resistance quantum,  $R_Q$ .

Our picture for local superconductivity connects the timescale of thermal fluctuations near quantum criticality,  $\tau = h/(k_B T)$ , to specific resistance. In the literature there is a widely hypothesized connection between the Planckian scattering time  $\tau_s = h/(k_B T)$  and quantum-critical metals [39–43]. Given recent reports of Planckian scattering in a superconductor-insulator system [36], and of the qualitative similarity of some of our specific resistance curves to Ref. [36], we were motivated to directly compare our data with a model of Planckian scattering. Following the method of Ref. [36], we computed  $T_P d\rho/dT$ , where the plasma temperature  $T_P$  plays the role of the high-temperature cutoff for superconducting behavior in our system. The Planckian bound is  $T_P \cdot d\rho/dT < h/(4e^2)$ . As shown in Fig. S15b, the observed resistance exceeds this bound by more than an order of magnitude. Thus, the Planckian bound apparently does not apply in our system.



## X. THEORY

Here we give an overview of the theoretical origin of power-law scaling discussed in the main text.

The key simplification for our case arises from the fact that the dimensionless phase slip fugacity,  $y \propto e^{-4\sqrt{2E_J/E_C}}$  is small, less than  $10^{-10}$  at zero magnetic field. This allows us to work with linearized renormalization group equations from Ref. [13], which in the long-screening-length limit ( $\Lambda \gg 1$ ) takes the form

$$\frac{dK}{dl} = -K(1 - u_g) \quad (S7)$$

$$\frac{du_g}{dl} = 2u_g(1 - u_g) \quad (S8)$$

$$\frac{dy}{dl} = \frac{1 + u_g}{2}(2 - \pi K)y. \quad (S9)$$

Here  $K$  is the superfluid stiffness, taking the initial value  $K_C = \sqrt{E_J/2E_C}$  and  $u_g$  takes the initial value  $1/(1 + \Lambda^2)$ , where  $\Lambda$  is the charge screening length, representing the plasmon group velocity in the UV limit in units of the plasma frequency. Following Ref. [13], we assume the renormalization flow is terminated at the thermal length given by  $e^l = \Omega_p/T$  where  $\Omega_p = \sqrt{2E_J E_C}$  is the single junction plasma frequency. The resistance is then given by  $R = R_0 y^2 / e^l$ .

Equations (S7-S8) express the renormalization of  $K$  from its ultraviolet value of  $K_C$  down to  $K_g$  at the fixed point  $u_g = 1$ .

In the high temperature limit where  $K$  is hardly renormalized, resistance follows the power law behavior

$$R = R_0 \left( \frac{T}{\Omega_p} \right)^{\pi K_C - 1}. \quad (S10)$$

At lower temperature  $K$  is renormalized down and the system crosses over to insulating behavior. The crossover temperature depends on system parameters,

$$T_{\text{ins}} = \max(2E_C/\pi, \sqrt{2E_J E_C}/\Lambda). \quad (S11)$$

The first case occurs in the limit of small Josephson energy, and insulating behavior appears because  $K$  is renormalized below  $1/\pi$ , at which point the system enters strong coupling. The second case occurs in the limit of large Josephson energy, and insulating behavior appears because the system crosses over to the infrared limit where  $u_g = 1$ , which is the case we focus on in the main text.

In the experiment, the two terms in Eq. S11 are actually comparable, so it is perhaps surprising that a square-root behavior is observed in Fig. 4a of the main text. As we caution in the main text, the experimentally extracted  $T^*$  may not map directly on to  $T_{\text{ins}}$ , and indeed different metrics give different quantitative behavior.

### A. Boundaries in theoretical phase diagram

The superconductor-insulator transition is strictly only a phase transition at  $T = 0$ ; otherwise it is a crossover [2]. The theoretical phase diagram in the main text in fact labels crossover boundaries, where the temperature dependence of the specific resistance  $d\rho/dT$  changes sign. To identify these points, we work perturbatively in the limit of small phase-slip fugacity, as discussed above.

At low temperatures where the infrared fixed-point of Eqs. (S7-S8) is reached, the  $\rho(T)$  power law is  $2\pi K_g - 3$ , which gives the low-temperature crossover  $\pi K_g \sim 3/2$ . Note that once terms of order  $y^2$  are included into Eq. S9, one would actually find either the Giamarchi-Schulz or BKT fixed points depending on if disorder is included [2, 23]. Since this correction is small compared to those associated with local superconductivity discussed in the main text, we simply indicate the crossover point with a  $\sim$  to avoid ambiguity.

By similar logic, in the high-temperature limit  $\rho(T)$  power law is  $\pi K_C - 1$ , which yields the local superconductor-insulator crossover  $\pi K_C \sim 1$ .

The boundary between local and global regimes is given by Eq. S11, which when smoothly interpolated yields the theoretical diagram in the main text.